

Multiple Peg-in-Hole Assembly of Tightly Coupled Multi-manipulator Using Learning-based Visual Servo

Jiawei Zhang, Chengchao Bai and Jifeng Guo

Abstract—Multiple peg-in-hole assembly is one of the fundamental tasks in robotic assembly. In the multiple peg-in-hole task for large-sized parts, it is challenging for a single manipulator to simultaneously align multiple distant pegs and holes, necessitating tightly coupled multi-manipulator systems. For such Multi-manipulator Multiple Peg-in-Hole (MMPiH) tasks, we propose a collaborative visual servo control framework that uses only the monocular in-hand cameras of each manipulator to reduce positioning errors. Initially, we train a state classification neural network and a positioning neural network. The former is used to divide the states of peg and hole in the image into three categories: obscured, separated and overlapped, while the latter determines the position of the peg and hole in the image. Based on these findings, we propose a method to integrate the visual features of multiple manipulators using virtual forces, which can naturally combine with the cooperative controller of the multi-manipulator system. To generalize our approach to holes of different appearances, we varied the appearance of the holes during the dataset generation process. The results confirm that by considering the appearance of the holes, classification accuracy and positioning precision can be improved. Finally, the results show that our method achieves an 85% success rate in dual-manipulator dual peg-in-hole tasks with a clearance of 0.2 mm.

I. INTRODUCTION

In recent years, robots have played an increasingly important role in automated assembly. Multiple peg-in-hole assembly is a fundamental operation in this context. This technology is involved in tasks ranging from on-orbit assembly of large space structures to precise assembly of small electronic components[1][2]. Currently, research on multiple peg-in-hole assembly tasks typically focuses on single manipulator assembly for small parts. However, as the size of the parts increases, it becomes challenging for a single manipulator to simultaneously align multiple distant pegs and holes. This necessitates tightly coupled cooperative assembly using multiple manipulators, as shown in Figure 1. This paper studies such MMPiH task.

Peg-in-hole task can be divided into two stages: hole searching and insertion. During the hole searching stage, the

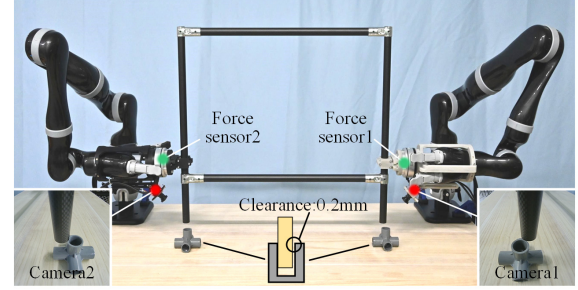


Figure 1. The Multi-manipulator Multiple Peg-in-Hole (MMPiH) task studied in this paper.

positioning uncertainty should be reduced to align the peg and hole. After the peg and hole are aligned, the insertion stage aims to complete the assembly compliantly while avoiding jamming. We focus on the hole search stage. For single peg-in-hole task, there are many methods to reduce positioning errors, such as reinforcement learning[3], imitation learning[4], Attractive Region In Environment (ARIE)[5], etc. These methods usually rely on contact force between the peg and hole to guide the hole searching process. However, in multiple peg-in-hole task for large-sized parts, contact force cannot provide guidance for hole search.

Different from the aforementioned methods, blind search[6] and visual servo[7] do not require contact force to guide the search, but the blind search method is time-consuming, and the classical visual servo method is sensitive to background, light and the shape variations. In recent years, learning-based visual servo has shown strong generalization performance through domain randomization technology.

Compared with the single manipulator assembly task, the visual servo system of the MMPiH task needs to integrate the visual features of multiple manipulators. To integrate the visual features of multiple manipulators and the cooperative controller, we propose a cooperative visual servo control framework based on virtual force. In summary, the main contributions of this paper are as follows:

- 1) For MMPiH task, a collaborative visual servo control framework is proposed. The positioning error can be quickly reduced by using only the monocular in-hand cameras of each manipulator.

- 2) A method is proposed to integrate the visual features of multiple manipulators based on virtual force. Deep learning is used to determine the relative state and position of the peg-hole pair in the images, these visual features are converted into the virtual force acting on the object.

- 3) Developed a new synthetic dataset for the peg-in-hole task, enhancing previous datasets by introducing variations in

*This work was co-supported by the Major Research Plan of the National Natural Science Foundation of China (No.92371111), Young Elite Scientists Sponsorship Program by CAST (No.2021QNRC001), Natural Science Foundation of Heilongjiang Province of China (No.YQ2022F012), Fundamental Research Funds for the Central Universities (Grant No. HIT.OCEF.2023010) and Siyuan Alliance Open ended Fund (HTKJ2022KL012003). (Corresponding author: Chengchao Bai).

Jiawei Zhang is with the school of Astronautics, Harbin Institute of Technology, China. (e-mail: j.zhang@stu.hit.edu.cn).

Chengchao Bai is with the school of Astronautics, Harbin Institute of Technology, China. (e-mail: baichengchao@hit.edu.cn).

Jifeng Guo is with the school of Astronautics, Harbin Institute of Technology, China.

hole appearances. Experimental results confirmed the importance of appearances for neural network training.

4) The submillimeter-level dual-hole assembly task is realized using tightly coupled dual-manipulator. To the best of our knowledge, this task has not been previously explored.

II. RELATED WORKS

A. Single Peg-in-Hole Assembly of Single Manipulator

There are many methods of hole search for single peg-in-hole task. Blind search using pre-designed search trajectories, such as spiral trajectories [6], Lissajous curves [8], or others, to explore areas where holes may exist. Such methods typically require a long time due to the absence of prior information about the hole position, and the time consumption increases with the misalignment between the peg and the hole.

The hole searching methods based on reinforcement learning typically take contact force and estimated hole position as input [3][9][10]. They define the action space as a set containing a limited number of action primitives, and train a neural network to select action primitives. Reinforcement learning often requires a large amount of interaction data for training, and there may be challenges in transferring learned models from a simulation environment to a real-world setting. Recent research shows that when there is overlap between the peg and hole, finite state machines can be used to select action primitives directly, which are simpler and more efficient [11].

Imitation learning is a technique that directly learns skills from demonstration data. Common methods include Dynamic Movement Primitives (DMPs) [12], Gaussian Mixture Regression (GMR) [4], deep learning [13][14], and so on. Compared with reinforcement learning, imitation learning has higher data efficiency, but it needs a lot of teaching data.

ARIE [5][15][16] is a concept inspired by human assembly, which automatically reduces the pose error between the peg and hole through environmental constraints. It utilizes low-precision force/torque sensors to accomplish high-precision assembly tasks. However, both finite state machine [11] and ARIE can only be employed when the end faces of the peg and hole overlap.

Visual servo [7] methods are able to reduce large pose error. However, classical visual servo methods require the identification of object features and are easily influenced by lighting and background clutter. In recent years, learning-based visual servo has demonstrated robust generalization performance through domain randomization techniques. Joshua et al. [17] used the VGG network to estimate the position of the hole and synthesized training images using domain randomization. They discretized the movement of the manipulator into finite motion directions to enhance the algorithm's robustness. In contrast, Rasmus et al. [18] simultaneously estimated the positions of both the peg and the hole. They aligned the peg and hole through continuous visual servo, which proved to be more efficient.

B. Multiple Peg-in-Hole Assembly of Single Manipulator

The research on the multiple peg-in-hole assembly of single manipulator has a long time. Sathirakul et al.[19] first studied the possible equilibrium states in two-dimensional dual-peg

insertions task, gave the geometric conditions and the force-torque equations of each equilibrium state, and obtained the jamming diagrams[20] and the taxonomy of dual-peg insertions. After that, Fei et al.[21] analyzed the three-dimensional multiple peg-in-hole assembly process, and Zhang et al.[22] analyzed the flexible dual peg-in-hole assembly process of flexible parts. The aforementioned researches studied the contact model in the multiple peg-in-hole task and the assembly strategy based on the contact model. Due to the complexity of the contact model in the multiple peg-in-hole task and the uncertainty in the assembly process, the assembly strategy not based on the contact model has received much attention in recent years [2][23][24]. The aforementioned researches typically focus on the insertion stage, which involves small-scale movements. Currently, there is limited literature addressing the hole searching stage in the context of multiple peg-in-hole assembly of single manipulator.

C. Single Peg-in-Hole Assembly of Multiple Manipulators

In multi-manipulator single peg-in-hole assembly task, one manipulator is typically designated as the assist arm, while the other serves as the task arm[6][25][26]. The assist arm is used to hold the part with the hole, whereas the task arm is used to hold the peg. In such assembly tasks, there are no closed-chain constraints between the assist arm and the task arm, resulting in a loosely coupled state. Lee et al.[6] used GMM to classify contact states in dual-arm cooperative assembly tasks, the joint torques of both the assist arm and the task arm are considered during classification. Alles et al.[25] used the model-free reinforcement learning to train a centralized policy in the simulation environment, which simultaneously controls the movements of the assist arm and the task arm, achieving direct transfer from simulation to reality. Correspondingly, Yao et al.[26] used multi-agent reinforcement learning algorithm to train distributed policies for the assist arm and the task arm.

In summary, although peg-in-hole tasks have been extensively studied, current work primarily focuses on single manipulator assembly of small-sized parts. Existing research on multi-manipulator cooperative assembly adopts loosely coupled assembly strategies. To the best of our knowledge, there has been no research on multiple peg-in-hole assembly for large-sized parts using tightly coupled multi-manipulator.

III. METHODS

A. Overview of the Method

The workflow of the proposed method is shown in Figure 2. It mainly consists of four parts: state classification neural network, positioning neural network, virtual force calculation module, and force controller for tightly coupled multi-manipulator.

Firstly, the states of the peg and hole in the images are categorized into three classes: obscured, separated and overlapped. The example images of the three types of states are shown in Figure 3. The state classification neural network is to determine the state of the peg and hole in the images, and the positioning neural network is to estimate the positions of the peg and hole in the images. Building upon this, we

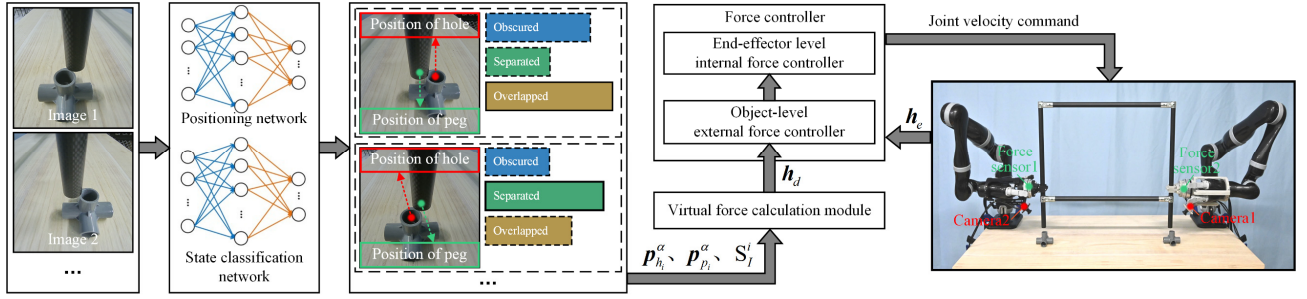


Figure 2. The workflow of the proposed method.

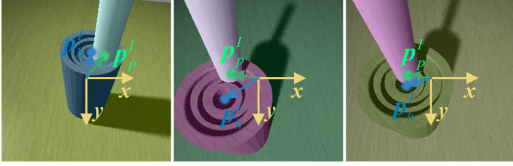


Figure 3. The image coordinate system and example images of the three types of states. From left to right: obscured, overlapped, and separated.

calculate the virtual force acting on the object, which is used as an input to the multi-manipulator cooperative controller to guide the object's motion. The multi-manipulator cooperative controller consists of two components: the object-level external force controller and the end-effector-level internal force controller. In the following, we will provide detailed explanations of these four components.

B. The State Classification Neural Network and Positioning Neural Network

1) *Network structure*: For the state classification neural network, we use the ImageNet pretrained VGG16. The neural network takes RGB images of size $224 \times 224 \times 3$ as input, and the output of the neural network is changed from 1000 dimensions to 3 dimensions. We train the neural network using the cross-entropy loss function.

For the positioning neural network, we use the ResNetUNet [18] (a U-Net architecture with an ImageNet pretrained ResNet18 backbone). Similar to [18], we utilize Gaussian kernel to convert the true positions of the peg and hole into heatmaps for training the neural network. We define the image coordinate system as shown in Figure 3. \mathbf{p}^I is used to represent any point in the image coordinate system, then the heat map corresponding to the target point \mathbf{p}_g^I can be expressed as:

$$\mathbf{H}_{p_g^I} = \exp\left(-\frac{\|\mathbf{p}^I - \mathbf{p}_g^I\|^2}{2\sigma^2}\right) \quad (1)$$

The positions of the peg and hole are represented as \mathbf{p}_p^I and \mathbf{p}_h^I in the image coordinate system. The positioning neural network takes RGB images of size $224 \times 224 \times 3$ as input and outputs estimated dual-layer heatmap $\hat{\mathbf{H}} = [\hat{\mathbf{H}}_{p_p^I}, \hat{\mathbf{H}}_{p_h^I}]$ of size $224 \times 224 \times 2$. We choose Mean Squared Error (MSE) as the loss function, and the truth heat map \mathbf{H} was used for supervised training. The positions of the maximum pixel values in each layer of the dual-layer heatmap are taken as the estimated positions of the peg and the hole:

$$\begin{cases} \hat{\mathbf{p}}_p^I = \operatorname{argmax}_{p^I} \hat{\mathbf{H}}_{p_p^I} \\ \hat{\mathbf{p}}_h^I = \operatorname{argmax}_{p^I} \hat{\mathbf{H}}_{p_h^I} \end{cases} \quad (2)$$

2) *Data generation*: The neural network in this paper is trained entirely on images generated by the simulator CoppeliaSim with POV-Ray render mode. To mitigate the influence of hole appearances, we built 14 scenes with different hole appearances, along with a control scene with flat hole. By randomizing the scene's color, light poses, camera poses, and peg poses, we generated 600 images for each hole appearance, comprising 200 images for each of the obscured, overlapped, and separated states. Some images of these 14 holes are shown in Figure 4. For the scene with the flat hole, we generated 1800 images, with 600 images allocated for each of the obscured, overlapped, and separated states. Some sample images of the flat hole are shown in Figure 5.

In the process of image generation, we uniformly randomly sample the RGB color of the desktop, peg, and hole, while making the color of the peg and hole the same with a probability of 50%. The angle between the direction of the light and the hole axis is set to 45 degrees. The light position is randomly selected on a circle 360 degrees around the hole axis. The distance between the peg and the hole is randomly selected in $[-0.05, -0.05, 0]$ m to $[0.05, 0.08, 0.05]$ m. The peg orientation error is sampled as an axis angle vector, where the axis is sampled from the surface of a unit sphere, and the angle is sampled between 0° and 10° . The distance between the camera and the hole is randomly selected between 0.1 m and 0.15 m, and the angle between the camera's optical axis and the hole surface is randomly selected between 35 degrees and 65 degrees to preliminarily determine the camera's initial pose. Subsequently, we randomly select the camera's position within a sphere centered at the initial camera position with a radius of 0.03 m. Based on the initial orientation of the camera, we introduce a pose error by adding a rotation angle of 10 degrees with a randomly chosen direction. The code generating the dataset are available at: <https://github.com/hit618/peg-in-hole-images-generator.git>.

C. Virtual Force Calculation Module

Suppose the number of manipulators is m . the position of the pegs and holes in the image coordinate system is denoted as $\mathbf{p}_{p_i}^I$ and $\mathbf{p}_{h_i}^I$ ($i=1, 2, \dots, m$). The position vectors of the pegs and holes in the camera coordinate system are denoted as $\mathbf{p}_{p_i}^c$ and $\mathbf{p}_{h_i}^c$ respectively, they can be calculated using the

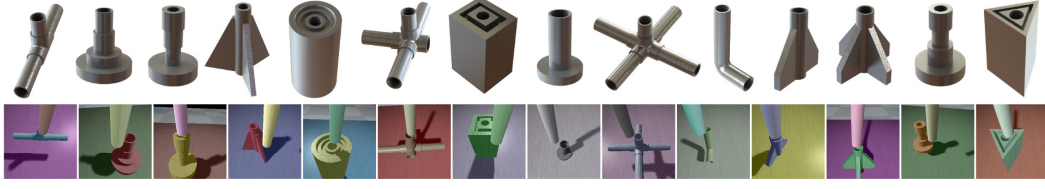


Figure 4. Up: the 14 holes used for generating images. Down: the images of scenes with different hole appearances. From left to right: hole1 to hole14.



Figure 5. Images of scene with flat hole.

camera's imaging model:

$$\mathbf{p}_{p_i}^c = \begin{bmatrix} \mathbf{p}_{p_i}^l \\ f \end{bmatrix} \begin{bmatrix} 1/\alpha_x & 0 & 0 \\ 0 & 1/\alpha_y & 0 \\ 0 & 0 & 1 \end{bmatrix} \quad (3)$$

$$\mathbf{p}_{h_i}^c = \begin{bmatrix} \mathbf{p}_{h_i}^l \\ f \end{bmatrix} \begin{bmatrix} 1/\alpha_x & 0 & 0 \\ 0 & 1/\alpha_y & 0 \\ 0 & 0 & 1 \end{bmatrix} \quad (4)$$

Where, α_x and α_y are scale coefficients, through which the pixel coordinates can be converted into metric unit, f is the focal length of the camera. Next, we can calculate the unit vectors \mathbf{n}_{p_i} and \mathbf{n}_{h_i} of $\mathbf{p}_{p_i}^c$ and $\mathbf{p}_{h_i}^c$ in the world coordinate system:

$$\begin{cases} \mathbf{n}_{p_i} = R_{c_i} \mathbf{p}_{p_i}^c / \|R_{c_i} \mathbf{p}_{p_i}^c\| \\ \mathbf{n}_{h_i} = R_{c_i} \mathbf{p}_{h_i}^c / \|R_{c_i} \mathbf{p}_{h_i}^c\| \end{cases} \quad (5)$$

Where, R_{c_i} is the rotation matrix representing the pose of the camera coordinate system relative to the world coordinate system, and the unit vector of the hole axis is represented as \mathbf{l} . \mathbf{p}_{c_i} represents the position of the origin of the camera coordinate system in the world coordinate system. Suppose the peg is fixed to the manipulator's end-effector, and \mathbf{p}_{cp_i} is the vector from camera position \mathbf{p}_{c_i} to the peg position \mathbf{p}_{p_i} . The diagram of the vectors are illustrated in Figure 6. Let α_i be the plane passing through \mathbf{p}_{p_i} and perpendicular to \mathbf{l} . $\mathbf{p}_{p_i}^{\alpha_i}$ and $\mathbf{p}_{h_i}^{\alpha_i}$ represent the intersection points of vectors \mathbf{n}_{p_i} and \mathbf{n}_{h_i} with plane α_i , respectively. $\mathbf{p}_{p_i}^{\alpha_i}$ and $\mathbf{p}_{h_i}^{\alpha_i}$ are calculated as follows:

$$\begin{cases} \mathbf{p}_{p_i}^{\alpha_i} = \mathbf{p}_{c_i} + \frac{\mathbf{p}_{cp_i} \cdot \mathbf{l}}{\mathbf{n}_{p_i} \cdot \mathbf{l}} \mathbf{n}_{p_i} \\ \mathbf{p}_{h_i}^{\alpha_i} = \mathbf{p}_{c_i} + \frac{\mathbf{p}_{cp_i} \cdot \mathbf{l}}{\mathbf{n}_{h_i} \cdot \mathbf{l}} \mathbf{n}_{h_i} \end{cases} \quad (6)$$

Finally, the deviation vector of the peg and hole on the plane α_i is calculated as:

$$\mathbf{d}_i = \mathbf{p}_{h_i}^{\alpha_i} - \mathbf{p}_{p_i}^{\alpha_i} = \frac{\mathbf{p}_{cp_i} \cdot \mathbf{l}}{\mathbf{n}_{h_i} \cdot \mathbf{l}} \mathbf{n}_{h_i} - \frac{\mathbf{p}_{cp_i} \cdot \mathbf{l}}{\mathbf{n}_{p_i} \cdot \mathbf{l}} \mathbf{n}_{p_i} \quad (7)$$

In the single manipulator assembly, we can directly use \mathbf{d}_i to calculate the direction of movement of the peg, but in the multi-manipulator assembly task, we need to comprehensively

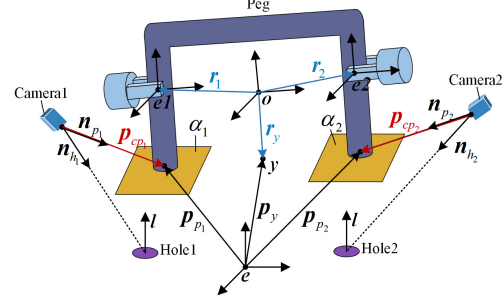


Figure 6. Schematic diagram of the vectors in the paper.

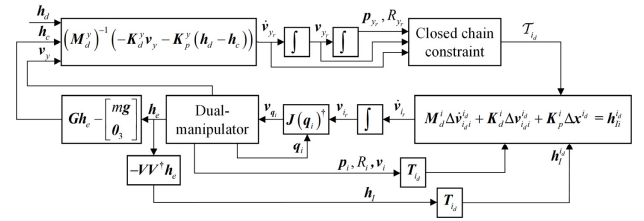


Figure 7. The control system block diagram of the cooperative controller.

consider the movement of the all pegs to calculate the overall movement of the assembled object. In this paper, we integrate the motion of all pegs in the form of virtual forces. The virtual forces acting on peg i is expressed as:

$$\mathbf{F}_i = k_F \frac{\mathbf{d}_i}{\max(\|\mathbf{d}_1\|, \|\mathbf{d}_2\|, \dots, \|\mathbf{d}_i\|)} \quad (8)$$

Where, k_F is the force gain coefficient. Since $\mathbf{p}_{p_i}^{\alpha_i}$ and $\mathbf{p}_{h_i}^{\alpha_i}$ are in a plane perpendicular to \mathbf{l} , the distance between the hole and plane α_i does not change under the action of \mathbf{F}_i . The virtual resultant forces \mathbf{F} and virtual resultant torque \mathbf{M} acting on the object are:

$$\begin{cases} \mathbf{F} = \mathbf{F}_\varepsilon + \sum_{i=1}^m \mathbf{F}_i \\ \mathbf{M} = \left(k_M \left(\sum_{i=1}^m \mathbf{r}_i \times \mathbf{F}_i \right) \cdot \mathbf{l} \right) \mathbf{l} \end{cases} \quad (9)$$

Where, k_M is the torque gain coefficient. In practice, when the value of $\sum \mathbf{F}_i$ is too small, the object will no longer move due to the effect of friction. To address this issue, a random term \mathbf{F}_ε is added to the resultant forces when the value of $\sum \mathbf{F}_i$ is too small.

$$\begin{cases} \mathbf{F}_\varepsilon = \mathbf{0} & \|\sum \mathbf{F}_i\| \geq F_s \\ \mathbf{F}_\varepsilon = k_\varepsilon (x\mathbf{F}_{O_1} + (1-x)\mathbf{F}_{O_2}) & \|\sum \mathbf{F}_i\| < F_s \end{cases} \quad (10)$$

Where, $x \sim \text{Bernoulli}(0.5)$, F_s is the threshold for applying random force, and k_ε is used to adjust the magnitude

of random force. F_{O_i} represents the direction of the random force, and since the random force is typically applied when occlusion occurs, we set F_{O_i} to be the direction that moves peg forward in the field of view, i.e.:

$$F_{O_i} = \frac{(-p_{cp_i} \cdot l)l + p_{cp_i}}{\|(-p_{cp_i} \cdot l)l + p_{cp_i}\|} \quad (11)$$

In the equation, $(-p_{cp_i} \cdot l)l + p_{cp_i}$ can be regarded as the projection of vector p_{cp_i} on the plane α_i . We divide the assembly process into two stages: before the contact between the pegs and the holes occurs, and after the contact occurs. Let h_d represent the desired virtual resultant forces and virtual resultant torque acting on the object, and let $S_l^i \in \{\text{Obscured}, \text{Separated}, \text{Overlapped}\}$ represent the relative state of the peg and hole in the image of manipulator i . The value of h_d is determined as follows:

$$\begin{cases} h_d = [F^T - k_F l^T, M^T]^T & \text{If contact} \\ h_d = [-k_F l^T, \theta_3]^T & \text{else if } S_l^1 = S_l^2 = \dots = S_l^i = \text{Overlapped} \\ h_d = [F^T, M^T]^T & \text{else} \end{cases} \quad (12)$$

θ_3 is a zero vector of size 1×3 . Before contact, if the images from all cameras are in overlapping state, the object is inserted along the axis of the hole. Otherwise, the object is moved in the direction that reduces the misalignment. After contact, while continuing to move in the direction that reduces the misalignment, we also to maintain a contact force $k_F l^T$ between the object and the hole.

D. Force Controller for Tightly Coupled Multi-manipulator

To ensure the safety of the assembly process, it is necessary to control not only the movement of the object under the action of the virtual forces h_d but also to keep the internal forces acting on the object within a limited range. To achieve this, we adopt a two-level control scheme. We use the direct force control algorithm for the object to generate reference motions for the manipulator's end-effector, and then use an end-effector-level internal force controller to generate joint velocity commands. The block diagram of the controller is shown in Figure 7. First, we select a control point y fixed to the object. Then, the reference acceleration of point y is computed using the following control law:

$$\dot{v}_{y_r} = (M_d^y)^{-1} (-K_d^y v_y - K_p^y (h_d - h_c)) \quad (13)$$

Where, $v_y = [\dot{p}_y^T, \dot{\omega}_y^T]^T$ represents the velocity of point y , $\ddot{v}_{y_r} = [\ddot{p}_{y_r}^T, \ddot{\omega}_{y_r}^T]^T$ is the reference acceleration of point y , $M_d^y \in \mathbb{R}^{6 \times 6}$, $K_d^y \in \mathbb{R}^{6 \times 6}$ and $K_p^y \in \mathbb{R}^{6 \times 6}$ respectively denote the desired object inertia matrix, damping matrix, and force feedback gain coefficient. All three matrices are chosen to be symmetric positive definite matrices, $h_c = [f_c^T, \mu_c^T]^T$ is the resultant force and resultant torque applied to the object by the environment. h_c can be estimated using force/torque sensors at the manipulator's end-effector. Assuming that the velocity and acceleration of the object are small during the assembly process, we ignore the inertial force and the velocity-dependent nonlinear forces of the object, that is:

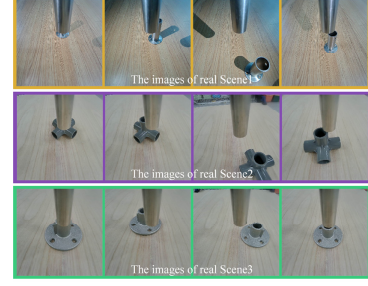


Figure 8. Example images from the dataset of real peg-in-hole scenes.

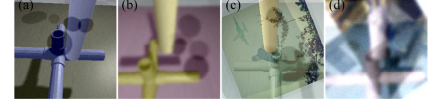


Figure 9. Examples of augmented images. (a)-(b) Images without overlaid natural images; (c)-(d) Images with overlaid natural images.

$$h_c = G h_e - \begin{bmatrix} mg \\ \theta_3 \end{bmatrix} \quad (14)$$

Where, m is the mass of the object. $h_e = [h_{e1}^T, h_{e2}^T, \dots, h_{ei}^T]^T \in \mathbb{R}^{6 \times m}$ represents the external force and external torque applied to all end-effectors. Here, $h_{ei} = [f_{ei}^T, \mu_{ei}^T]^T$ denotes the external force and external torque applied to the end-effector of manipulator i , which can be measured by force/torque sensors, and G is the grasp matrix.

$$G = \begin{bmatrix} I_3 & \theta_{3 \times 3} & \dots & I_3 & \theta_{3 \times 3} \\ r_1 \times I_3 & I_3 & \dots & r_i \times I_3 & I_3 \end{bmatrix} \quad (15)$$

Where, G is usually row full rank, by inverting G , the relationship between the resultant force h_o acting on the object's center of mass and the h_e is as follows:

$$-h_e = G^\dagger h_o + V h_n = h_E + h_I \quad (16)$$

Where, $G^\dagger \in \mathbb{R}^{6 \times 6}$ is the pseudo-inverse of the matrix G , the column vector of the matrix $V \in \mathbb{R}^{6 \times 6}$ spans the null space of the matrix G , h_n is the internal force acting on the object, which does not induce motion of the object, h_E and h_I respectively denote the components of $-h_e$ that generate the motion and the internal force of the object. For a given h_e , h_I can be calculated by:

$$h_I = [(h_{I1})^T, (h_{I2})^T, \dots, (h_{In})^T]^T = -V V^\dagger h_e \quad (17)$$

Integrating \dot{v}_{y_r} yields the reference motion \mathcal{T}_{y_r} of the object, which is composed of $p_{y_r}, R_{y_r}, v_{y_r}, \dot{v}_{y_r}$. Assuming no relative motion between the manipulator's end-effector and the object, the desired motion \mathcal{T}_{id} of the manipulator's end-effector and the reference motion \mathcal{T}_{y_r} of the object satisfy the following constraints:

$$\begin{cases} p_{id} = p_{y_r} + r_{yi} \\ R_{id} = R_{y_r} R_{y_i}^i \\ \dot{p}_{id} = \dot{p}_{y_r} - r_{yi} \times \omega_{y_r} \\ \omega_{id} = \omega_{y_r} \\ \ddot{p}_{id} = \ddot{p}_{y_r} - \omega_{y_r} \times r_{yi} \times \omega_{y_r} - r_{yi} \times \dot{\omega}_{y_r} \\ \dot{\omega}_{id} = \dot{\omega}_{y_r} \end{cases} \quad (18)$$

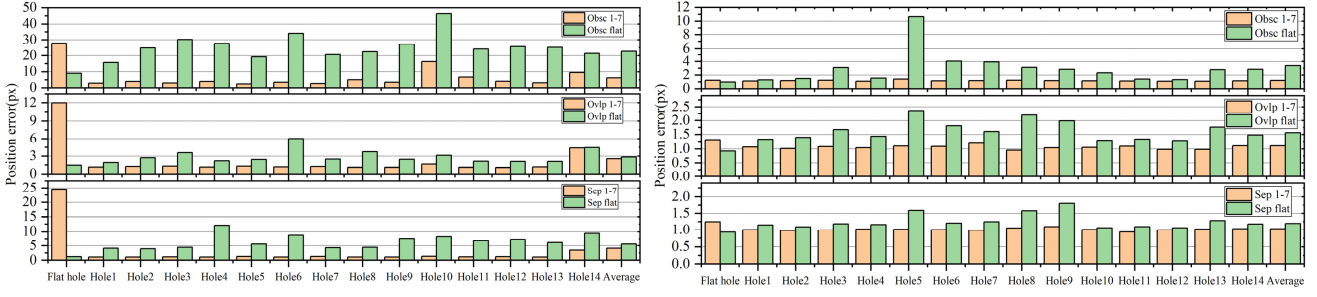


Figure 10. The test results of positioning errors. Left: the positioning errors of the hole. Right: the positioning errors of the peg. Obsc 1-7: Images in the obscured state with models trained on hole 1-7; Sep 1-7: Images in the separated state with models trained on hole 1-7; Ovlp 1-7: Images in the overlapped state with models trained on hole 1-7; Obsc flat: Images in the obscured state with models trained on flat hole; Sep flat: Images in the separated state with models trained on flat hole; Ovlp flat: Images in the overlapped state with models trained on flat hole.

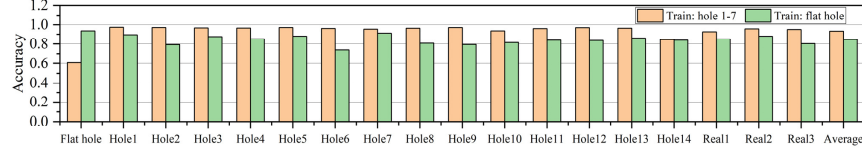


Figure 11. The average classification accuracy of the state classification neural network for images in all states.

Where, $\mathbf{r}_{yi} = \mathbf{r}_i - \mathbf{r}_y$, \mathbf{R}_y^i is the rotation matrix of the manipulator's end-effector with respect to the coordinate system of point y . $\mathbf{v}_{id} = [\dot{\mathbf{p}}_{id}^T, \dot{\boldsymbol{\omega}}_{id}^T]^T$ represents the desired velocity of the manipulator's end-effector, $\dot{\mathbf{v}}_{id} = [\ddot{\mathbf{p}}_{id}^T, \ddot{\boldsymbol{\omega}}_{id}^T]^T$ represents the desired acceleration of the end-effector. the desired motion \mathcal{T}_{id} of the manipulator's end-effector composed of $\mathbf{p}_{id}, \mathbf{R}_{id}, \mathbf{v}_{id}, \dot{\mathbf{v}}_{id}$. To control the internal forces acting on the object, we use the following end-effector-level impedance controller:

$$\mathbf{M}_d^i \Delta \mathbf{v}_{id}^{id} + \mathbf{K}_d^i \Delta \mathbf{v}_{id}^{id} + \mathbf{K}_p^i \Delta \mathbf{x}^{id} = \mathbf{h}_{fi}^{id} \quad (19)$$

In the equation, $\mathbf{M}_d^i \in \mathbf{R}^{6 \times 6}$, $\mathbf{K}_d^i \in \mathbf{R}^{6 \times 6}$ and $\mathbf{K}_p^i \in \mathbf{R}^{6 \times 6}$ represent the desired inertia matrix, damping matrix and stiffness matrix of the manipulator's end-effector, respectively, all chosen to be symmetric positive definite matrices. $\Delta \mathbf{x}^{id}$ represents the difference between the actual pose and the desired pose of the end-effector of the manipulator i . Similarly, $\Delta \mathbf{v}_{id}^{id} = \mathbf{T}_{id}(\mathbf{v}_i - \mathbf{v}_{id})$ represents the difference between the actual and desired velocity, $\Delta \dot{\mathbf{v}}_{id}^{id} = \mathbf{T}_{id}(\dot{\mathbf{v}}_i - \dot{\mathbf{v}}_{id})$ represents the difference between the reference acceleration and the desired acceleration. $\mathbf{h}_{fi}^{id} = \mathbf{T}_{id}^T \mathbf{h}_{fi}$ is the component of the force/torque applied by the end-effector to the object that generates internal force/torque within the object. \mathbf{T}_{id} is the transformation matrix, and after transformation, the above variables are expressed in the desired pose coordinate system Σ_{id} . The formulas for calculating \mathbf{T}_{id} and $\Delta \mathbf{x}^{id}$ are as follows:

$$\mathbf{T}_{id} = \begin{bmatrix} (\mathbf{R}_{id})^T & \mathbf{0}_{3 \times 3} \\ \mathbf{0}_{3 \times 3} & (\mathbf{R}_{id})^T \end{bmatrix} \quad (20)$$

$$\Delta \mathbf{x}^{id} = \begin{bmatrix} \mathbf{R}_{id}^T (\mathbf{p}_i - \mathbf{p}_{id}) \\ \mathbf{E}_{id} \end{bmatrix} \quad (21)$$

Where, \mathbf{E}_{id} represents the Euler angle corresponding to $\mathbf{R}_{id}^T \mathbf{R}_i$. Finally, the internal force/torque component \mathbf{h}_{fi} , the expected desired motion \mathcal{T}_{id} of the end-effector, the actual state information $\mathbf{p}_i, \mathbf{R}_i, \dot{\mathbf{p}}_i, \boldsymbol{\omega}_i$ of the end-effector, and the

impedance parameters $\mathbf{M}_d^i, \mathbf{K}_d^i, \mathbf{K}_p^i$ are substituted into equation (19)-(21) to calculate the reference acceleration $\dot{\mathbf{v}}_i = [\ddot{\mathbf{p}}_i^T, \ddot{\boldsymbol{\omega}}_i^T]^T$ of the manipulator's end-effector. The reference velocity \mathbf{v}_i of the end-effector is obtained by integrating $\dot{\mathbf{v}}_i$. Then, the reference joint velocity is calculated as follows:

$$\mathbf{v}_{qi} = \mathbf{J}(\mathbf{q}_i)^\dagger \mathbf{v}_i \quad (22)$$

Where, $\mathbf{q}_i \in \mathbf{R}^7$ is the joint angle vector of the manipulator (7-DOF redundant manipulator used in this paper), and $\mathbf{J}(\mathbf{q}_i)^\dagger \in \mathbf{R}^{7 \times 6}$ represents the pseudoinverse of the Jacobian matrix of the manipulator. \mathbf{v}_{qi} is the joint velocity command of the manipulator i .

IV. EXPERIMENTS

In this section, we first test the classification accuracy and the positioning error for different holes. Subsequently, the success rate and time consumption of the collaborative visual servo control framework were tested in two MMPiH tasks.

A. Training Details

We selected images from the generated simulation images to create two training datasets. The first training dataset consists of a total of 2100 images, all from scenes with holes 1-7. For each hole's 600 images, we selected 300 for training, with 100 images each for obscured, separated, and overlapped states. The second training dataset consists of a total of 1500 images, all from the flat hole scene, with 500 images each for obscured, separated, and overlapped states. The images not used for training will serve as the test dataset. Additionally, we collected images from three real peg-in-hole scenes to test the classification neural network, each containing 300 images, with 100 images each for obscured, separated, and overlapped states. We name the three real datasets as: Real 1-3, and some images of them are shown in Figure 8.

To mitigate the influence of background clutter, similar to [18], we random select natural images from the MS COCO dataset during training. These natural images are then

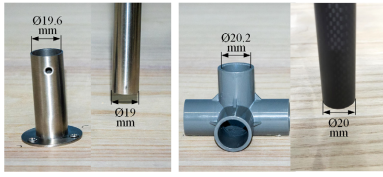


Figure 12. The holes and pegs used in the experiments. Left: the Hole1 and Peg1. Right: the Hole2 and Peg2.

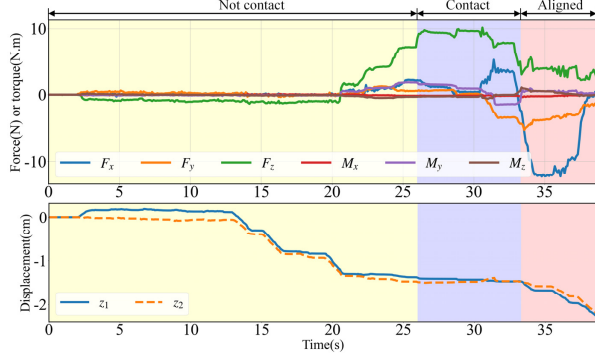


Figure 13. The state information during the assembly process, different background colors indicate different contact stages. Up: the estimated contact force/torque \mathbf{h}_c between the peg and the hole. Down: the displacement of the two end-effectors in the direction of the hole's axis (the hole's axis coincides with the z-axis of the world coordinate system).

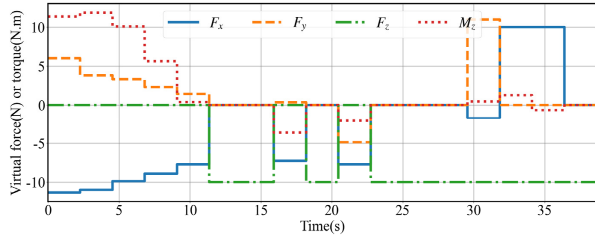


Figure 14. The virtual force/torque \mathbf{h}_d acting on the object during the assembly process.

randomly rotated and overlaid onto the simulated images with a probability of 50%. Additionally, we introduce ISO noise, Gaussian noise, and Gaussian blur to the images, and randomly adjust brightness, contrast, and saturation. The augmented images are shown in Figure 9. We also horizontally flip images with a 50% probability. We trained each model for 30 epochs with a batch size of 8, a maximum learning rate of 0.001, weight decay of 0.0001, and the optimizer is Adam. Training is conducted on an NVIDIA GeForce RTX 3090. When using the dataset of hole 1-7, it took about 18 minutes for state classification network and about 15 minutes for positioning network.

C. Positioning Accuracy

We trained the positioning neural network 5 times on each dataset separately, and calculated the average positioning errors for the hole and the peg for these five models. The results are shown in Figure 10. Since the hole may be obscured by the peg and the hole's position has greater uncertainty, positioning the hole is more challenging than positioning the peg. When the image is in obscured state, the positioning error for the hole is significantly greater than for other states. Models trained on holes 1-7 achieve better positioning accuracy for different holes. However, models trained on the

TABLE I. THE PARAMETERS OF THE CONTROLLER

Parameters	Value	Parameters	Value	Parameters	Value
k_F	10	\mathbf{M}_d^y	$10\mathbf{I}_6$	\mathbf{M}_d^i	$50\mathbf{I}_6$
k_M	2	\mathbf{K}_d^y	$1000\mathbf{I}_6$	\mathbf{K}_d^i	$100\mathbf{I}_6$
k_e	8	\mathbf{K}_p^y	$10\mathbf{I}_6$	\mathbf{K}_p^i	$50\mathbf{I}_6$

TABLE II. THE EXPERIMENTAL RESULTS

	Success rate	Average time	Max time	Min time
Hole1	19/20	40.87s	56.38s	22.24s
Hole2	17/20	48.18s	102.71s	27.52s

flat hole dataset only show advantage in flat hole scenes.

B. Classification Accuracy

We compared the classification accuracy of the neural network models trained on two datasets in various hole appearances. We also train 5 times for each dataset and the average results of these five neural network models are shown in Figure 11. It can be seen that models trained on scenes with hole1-7 can achieve better classification accuracy on different holes. Models trained on flat hole only show advantages in the flat hole scene, and do not generalize well in other scenes.

D. Peg-in-hole Performance

We conducted assembly experiments using two Kinova Jaco2 manipulators, as illustrated in Figure 1. Each manipulator equipped with a force/torque sensor and a monocular in-hand camera. We did experiments on two holes with different appearances, as shown in Figure 12, with inner diameters of 19.6mm and 20.2mm respectively, and pegs diameters of 19mm and 20mm respectively. We randomly select the initial positions of two pegs at a height of 1cm from the hole surface and within a range of 3cm from the center of the hole to generate a total of 20 initial poses of objects. If the assembly could not be completed within 40 steps (approximately 100 seconds), the assembly was considered failed. The threshold F_s is set to 5N, other parameters are shown in TABLE II.

We recorded the success rate and time consumption for the experiments, as shown in TABLE II. It can be seen that our method achieves a high success rate in a relatively short time. With an increase in assembly precision, there is a slight decrease in the assembly success rate and a slight increase in assembly time. Next, we selected one successful assembly process from the experiments of hole 2 for detailed analysis. Figure 13. shows the estimated contact force \mathbf{h}_c between the object and the hole during the assembly process, as well as the displacement of the two end-effectors in the direction of the hole's axis. It can be seen that the stable and compliant contact force control was achieved during the assembly process. Figure 14. shows the virtual force \mathbf{h}_d acting on the object during the assembly process. Since the hole's axis coincides with the z-axis of the world coordinate system, the virtual torque is applied only around the z-axis. The images in the assembly process and the output of the state classification neural network and the positioning neural network are shown in the Figure 15. It can be seen that the positioning accuracy of the peg and the hole is high in the assembly process. Although there are some classification errors, the impact is limited.

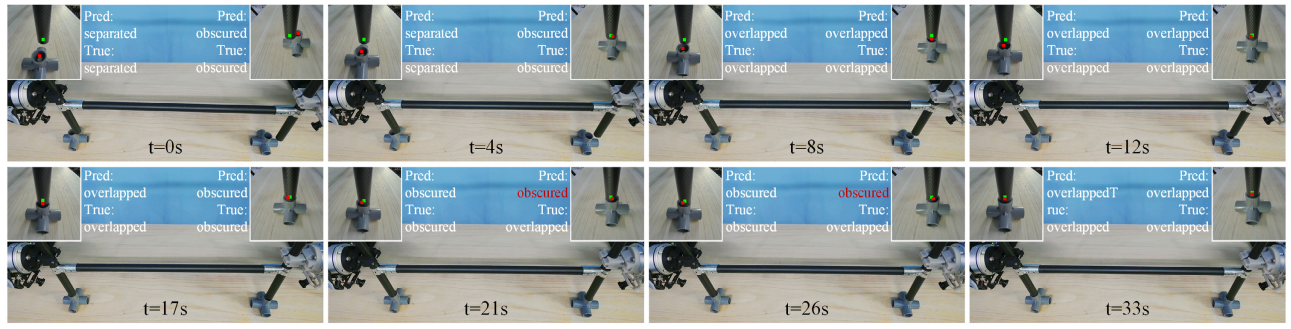


Figure 15. Some key frames of the assembly process, and the results from the state classification neural network and the positioning neural network.

V. CONCLUSION

In multiple peg-in-hole task for large-sized parts, contact force cannot provide guidance for hole search. In this paper, we using only the monocular in-hand cameras of each manipulator to reduce positioning errors. We constructed a new images dataset for peg-in-hole task and proposed a learning-based collaborative visual servo control framework for tightly coupled multi-manipulator. Our method successfully achieved submillimeter-level dual-manipulator dual-hole assembly task. We noticed that the classification neural network is affected by the reflection on the surface of the peg and hole. In future research, performance could be further improved by synthesizing more realistic simulated images.

ACKNOWLEDGMENT

The authors would like to thank the reviewers for the comments and suggestions, and the editor for significantly improving the paper.

REFERENCES

- [1] D. Li, L. Zhang, W. Zhu, Z. Xu, Q. Tang, and W. Zhan, "A survey of space robotic technologies for on-orbit assembly," *Space Sci Technol.* 2022.
- [2] Z. Hou, Z. Li, C. Hsu, K. Zhang, and J. Xu, "Fuzzy Logic-Driven Variable Time-Scale Prediction-Based Reinforcement Learning for Robotic Multiple Peg-in-Hole Assembly," *IEEE Trans. Autom. Sci. Eng.*, vol. 19, no. 1, pp. 218-229, 2022.
- [3] M. Oikawa, T. Kusakabe, K. Kutsuzawa, S. Sakaino, and T. Tsuji, "Reinforcement Learning for Robotic Assembly Using Non-Diagonal Stiffness Matrix," *IEEE Robot. Autom. Lett.*, vol. 6, pp. 2737-2744, 2021.
- [4] T. Tang, H. C. Lin, Y. Zhao, Y. Fan, W. Chen, and M. Tomizuka, "Teach industrial robots peg-hole-insertion by human demonstration," *IEEE ASME Int Conf Adv Intellig Mechatron AIM*, pp. 488-494, 2016.
- [5] H. Qiao, M. Wang, J. Su, S. Jia, and R. Li, "The concept of "attractive region in environment" and its application in high-precision tasks with low-precision systems," *IEEE-ASME Trans. Mechatron.*, vol. 20, no. 5, pp. 2311-2327, 2014.
- [6] H. Lee, S. Park, K. Jang, S. Kim, and J. Park, "Contact state estimation for peg-in-hole assembly using gaussian mixture model," *IEEE Robot. Autom. Lett.*, vol. 7, no. 2, pp. 3349-3356, 2022.
- [7] B. Thuilot, P. Martinet, L. Cordesses, and J. Gallice, "Position based visual servoing: keeping the object in the field of vision," *Proc IEEE Int Conf Rob Autom*, pp. 1624-1629, 2002.
- [8] M. Jokesch, J. Suchý, A. Winkler, A. Fross, and U. Thomas, "Generic algorithm for peg-in-hole assembly tasks for pin alignments with impedance controlled robots," *Adv. Intell. Sys. Comput.*, pp. 105-117, 2016.
- [9] T. Inoue, G. D. Magistris, A. Munawar, T. Yokoya, and R. Tachibana, "Deep reinforcement learning for high precision assembly tasks," *IEEE Int Conf Intell Rob Syst*, pp. 819-825, 2017.
- [10] S. Hoppe, M. Giftthaler, R. Krug, and M. Toussaint, "Sample-efficient learning for industrial assembly using qgraph-bounded ddpq," *IEEE Int Conf Intell Rob Syst*, pp. 9080-9087, 2020.
- [11] Wang C, Luo H, Zhang K, H. Chen, J. Pan, and W. Zhang, "POMDP-Guided Active Force-Based Search for Robotic Insertion," *IEEE Int Conf Intell Rob Syst*, pp. 10668-10675, 2023.
- [12] T. Davchev, K. S. Luck, M. Burke, et al. "Residual learning from demonstration: Adapting dmps for contact-rich manipulation," *IEEE Robot. Autom. Lett.*, vol. 7, no. 2, pp. 4488-4495, 2022.
- [13] Y. Liu, D. Romeres, D. K. Jha, and D. Nikovski, "Understanding multi-modal perception using behavioral cloning for peg-in-a-hole insertion tasks," *arXiv preprint arXiv:2007.11646*, 2020.
- [14] S. Gubbi, S. Kolathaya, and B. Amrutur, "Imitation learning for high precision peg-in-hole tasks," *Int. Conf. Control, Autom. Robot.*, pp. 368-372, 2020.
- [15] X. Li, R. Li, H. Qiao, C. Ma, and L. Li, "Human-inspired compliant strategy for peg-in-hole assembly using environmental constraint and coarse force information," *IEEE Int Conf Intell Rob Syst*, pp. 4743-4748, 2017.
- [16] Li R and Qiao H, "Condition and strategy analysis for assembly based on attractive region in environment," *IEEE-ASME Trans. Mechatron.*, vol. 22, no. 5, pp. 2218-2228, 2017.
- [17] J. C. Triyonoputro, W. Wan, and K. Harada, "Quickly inserting pegs into uncertain holes using multi-view images and deep network trained on synthetic data," *IEEE Int Conf Intell Rob Syst*, pp. 5792-5799, 2019.
- [18] R. L. Haugaard, J. Langaa, C. Sloth, and A. G. Buch, "Fast robust peg-in-hole insertion with continuous visual servoing," *Conf Rob Learn (CORL)*, 2020.
- [19] K. Sathirakul, and R. H. Sturges, "Jamming conditions for multiple peg-in-hole assemblies," *Robotica*, v10. 16, no. 3, pp. 329-345, 1998.
- [20] D. E. Whitney, "Quasi-static assembly of compliantly supported rigid parts," *J. Dyn. Sys., Meas., Control.*, vol. 104, no. 1, pp. 65-77, 1982.
- [21] Y. Fei, and X. Zhao, "An assembly process modeling and analysis for robotic multiple peg-in-hole," *J. Intell. Robot. Syst.*, vol. 36, pp. 175-189, 2003.
- [22] K. Zhang, J. Xu, H. Chen, J. Zhao, and K. Chen "Jamming analysis and force control for flexible dual peg-in-hole assembly," *IEEE Trans. Ind. Electron.*, vol. 66, no. 3, pp. 1930-1939, 2019.
- [23] J. Xu, Z. Hou, W. Wang, B. Xu, K. Zhang, and K. Chen, "Feedback Deep Deterministic Policy Gradient With Fuzzy Reward for Robotic Multiple Peg-in-Hole Assembly Tasks," *IEEE Trans. Ind. Inform.*, vol. 15, no. 3, pp. 1658-1667, 2019.
- [24] Y. Ma, D. Xu and F. Qin, "Efficient Insertion Control for Precision Assembly Based on Demonstration Learning and Reinforcement Learning," *IEEE Trans. Ind. Inform.*, vol. 17, no. 7, pp. 4492-4502, 2021.
- [25] M. Alles and E. Aljalbout, "Learning to Centralize Dual-Arm Assembly," *Front. Robot. AI*, 9:830007, 2022.
- [26] J. Yao, X. Wang, R. Li, W. Wang, X. Ping, and Y. Liu, "Dual manipulator collaborative shaft slot assembly via MADDPG," *2022 IEEE Int. Conf. Robot. Biomimetics*, pp. 1047-1052, 2022.